Book title

Yifan Sun
Department of Information Engineering, Electronics and Telecommunications
Sapienza University of Rome
Via Eudossiana 18, 00184 Rome, Italy

Pedro Parra-Rivas
Department of Information Engineering, Electronics and Telecommunications
Sapienza University of Rome
Via Eudossiana 18, 00184 Rome, Italy

Mario Zitelli
Department of Information Engineering, Electronics and Telecommunications
Sapienza University of Rome
Via Eudossiana 18, 00184 Rome, Italy

Fabio Mangini
Department of Information Engineering, Electronics and Telecommunications
Sapienza University of Rome
Via Eudossiana 18, 00184 Rome, Italy

Mario Ferraro
Department of Information Engineering, Electronics and Telecommunications
Sapienza University of Rome
Via Eudossiana 18, 00184 Rome, Italy

Stefan Wabnitz
Department of Information Engineering, Electronics and Telecommunications
Sapienza University of Rome
Via Eudossiana 18, 00184 Rome, Italy

Chapter 1

An introduction to guided-wave nonlinear ultrafast photonics

ABSTRACT

We present a general theoretical framework for describing ultrashort pulse propagation in optical fibers, and discuss the conditions for the generation of spatiotemporal bullets and multimode solitons. We compare theory with recent experiments involving the generation of multimode solitons in graded index multimode optical fibers. This reveals the formation of walk-off solitons, where nonlinearity compensates for both chromatic and modal dispersion, as well as the irreversible attraction of multimode solitons to the fundamental mode of the fiber for long propagation distances.

KEYWORDS

Optical fibers, Kerr effect, Optical solitons, Ultrashort pulses, Raman scattering

1.1 INTRODUCTION

Optical fibers are the most representative example of waveguides that support multiple transverse guided modes for a given optical frequency and state of polarization. In Sec. 1.2 , we discuss the basic properties of multimode fibers by comparing the two main examples: graded-index and step-index fibers. To inspect their mode properties, we present their eigenmodes and eigenvalues based on the different refractive index distributions. Next, we introduce the generalized multimode nonlinear Schrödinger equations, which describe the evolution of ultrashort optical pulses in fibers.

In Sec. 1.3 we will review some results regarding the formation of spatio-temporal solitons (STSs) in inhomogeneous (i.e., multimode) systems. Using a suitable parameter dependent STS ansatz, we compute the effective Lagrangian of the system, and reduce the infinite dimensional 3D+1 NLS to a 4D dynamical system describing the evolution of the ansatz parameters. In this context, the equilibria of this system correspond to shape preserving STSs. We study these point and their stability in two different regimes of operation.

In Sec. 1.4, the soliton solutions of the generalized nonlinear Schrödinger equations are presented, for the cases of single-mode and multimode fibers. We describe these solutions with the help of analytical formulas, which we compare with both numerical solutions and recent experiments. An interesting property which is peculiar to multimode solitons, is that they only form whenever the distances associated with various physical effects, specifically chromatic dispersion, modal dispersion, and Kerr nonlinearity, are all of the same order. In this situation, temporal broadening induced by chromatic dispersion and modal dispersion can be perfectly balanced by self- and cross-phase modulation induced by Kerr nonlinearity. We also point out that, for long propagation distances which are typical of telecom applications, an irreversible transfer of energy from higher-order modes into the fundamental mode is observed. As a result, multimode solitons are attracted into a single-mode soliton carried by the fundamental mode of the fiber.

1.2 GUIDED MODES IN OPTICAL FIBERS

1.2.1 introduction

In this subsection, we present the basic properties of multimode fibers (MMF), by comparing graded-index fibers (GIF) and step-index fibers (SIF). The different refractive index distributions of the two fibers result in very different eigenmodes and eigenvalues. On the one hand, the shape and size of their eigenmodes play a crucial role in determining the nonlinear strength of each mode, as well as the coupling among modes. On the other hand, the different orders of dispersion, derived from the eigenvalues, determine the fundamental propagation characteristics of the guided light field, such as phase velocity, group velocity, and group velocity dispersion. At the end of this subsection, we introduce the model of generalized multimode nonlinear Schrödinger equations.

1.2.2 Multimode fiber mode properties

The properties of multimode fibers are determined by the features of their eigenmodes. In the following part, we introduce the properties (nonlinearity and dispersion) of SIFs and GIFs, by comparing their eigenmodes and eigenvalues.

1.2.2.1 Fiber eigenmodes and effective modal indices

The first factor that determines fiber features is the fiber eigenmode profile. In this subsection, we introduce fiber eigenmodes by means of the two examples of a SIF or a GIF, with the same core size.

We start with SIFs. For such fibers, the refractive index in the longitudinal direction is homogeneous, but in the transverse section, the fiber core with refractive index n_{co} is wrapped by the fiber cladding with refractive index n_{cl}, where the index difference $\Delta n = n_{\mathrm{co}} - n_{\mathrm{cl}} > 0$. The transverse refractive index profile of SIFs is radially symmetric, and is given by

$$n(x, y, \lambda) = \begin{cases} n_{\mathrm{cl}}(\lambda) + \Delta n, & x^2 + y^2 < R^2 \\ n_{\mathrm{cl}}(\lambda), & x^2 + y^2 > R^2 \end{cases}, \tag{1.1}$$

where R is the core radius. Whenever the SIF core is made by undoped silica, the Sellmeier equation can be used to calculate wavelength dependent refractive index $n_{\mathrm{cl}}(\lambda)$ at the chosen wavelength λ [1]. For a SIF with radius $R = 25\,\mu$m and index difference $\Delta n = 0.0137$, we plot the index profile $n(x, y = 0, \lambda = 1.45\mu\mathrm{m})$ as in Fig. 1.1(a).

Light propagates along the longitudinal direction in fibers, but is transversely confined in the center core due to its higher refractive index with respect to the cladding. This confinement adds the boundary condition for fields in the transverse section, leading to guided propagation modes. Therefore, the fiber refractive index distribution (waveguide structure) fixes the properties of these modes at a given wavelength. On the other hand, the wavelength dependence of modes plays an important role in determining fiber properties. Generally, the shorter the wavelength, the more modes can be guided. For long wavelengths, there may be only a single guided mode. In this case, the fiber is the single mode for such an optical wavelength.

Based on the fiber profiles in Fig. 1.1(a) and parameters that we defined before, by using the semi-vectorial finite difference method [2], the first fifteen eigenmodes $F(x, y, \lambda_s)$ at $\lambda_s = 1.55\,\mu$m are plotted and marked as linearly polarized (LP) modes on the top of Fig. 1.1. These modes can be indexed by number m and l: m is the azimuthal index; l represents radial index; Degenerate modes with the same m, l are labeled by a, b. For compactness of notation, here we use the mode index p to refer to these modes. To compare the size of modes with the refractive index profile, the mode profile $F_p(x, y = 0)$ for mode $p = 1,\ 6,\ 15$ is plotted in Fig. 1.1(a). As we can see, the modes are well localized inside the core.

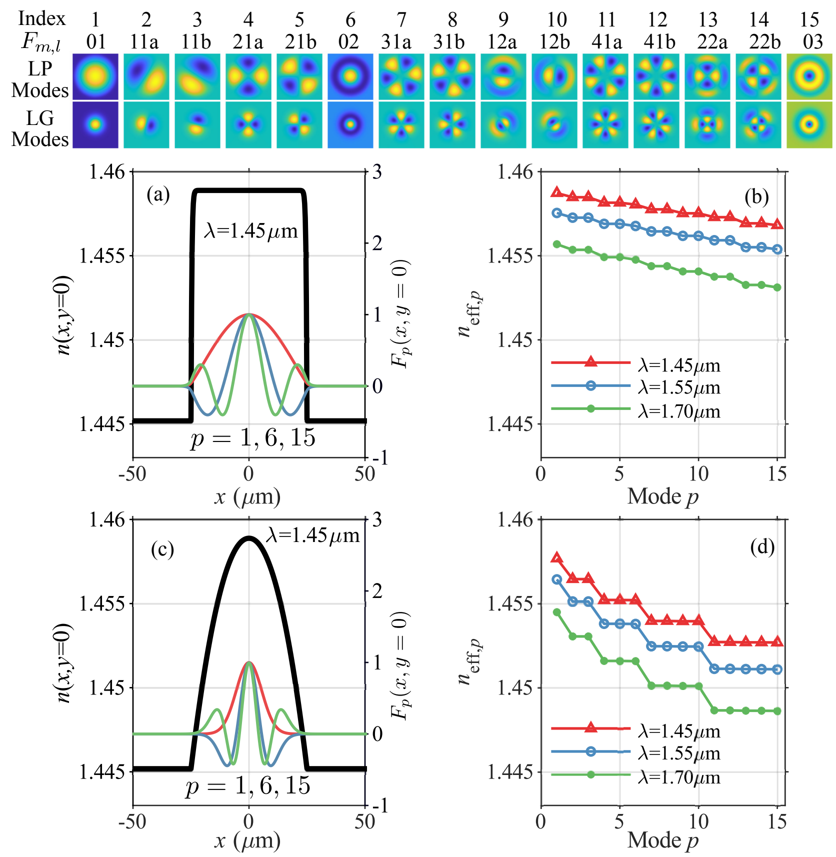

FIGURE 1.1 Refractive index profiles $n(x, y = 0)$ (black solid line) of SIF in (a,b) and GIF in (c,d) and their corresponding eigenmode profiles $F_p(x, y = 0)$, modal effective indices $n_{\mathrm{eff},p}$. The fiber radius for both fibers is $R = 25\ \mu$m.

As the refractive index changes, the guided modes also change. By taking the GRIN fiber with the same core size $R = 25\ \mu$m as an example, the refractive index has a parabolic distribution, which can be written as

$$n(x, y, \lambda) = \begin{cases} n_{\mathrm{cl}}(\lambda) + \Delta n \cdot \left(1 - \frac{x^2+y^2}{R^2}\right), & x^2 + y^2 < R^2 \\ n_{\mathrm{cl}}(\lambda), & x^2 + y^2 > R^2 \end{cases} . \tag{1.2}$$

The eigenmode profiles for this parabolic index profile are the Laguerre-Gauss (LG) modes. The fiber refractive index distribution $n(x, y = 0, \lambda = 1.45\mu\mathrm{m})$ and LG mode profiles $F_p(x, y = 0)$ for mode $p = 1,\ 6,\ 15$ are plotted in Fig. 1.1(c). It is clear that the modes in Fig. 1.1(a,c) are also almost fully localized inside the fiber core, but the effective area of the GIF is smaller than that of the SIF.

To characterize the mode sizes, we use their mode effective areas (MEAs)

$$A_{\text{eff, mode}\,p} = \frac{\left(\int\int |F_p(x,y)|\mathrm{d}x\mathrm{d}y\right)^2}{\int\int |F_p(x,y)|^4\mathrm{d}x\mathrm{d}y}. \tag{1.3}$$

Since the nonlinear coefficient of a fiber is inversely proportional to the MEA, the MEA is an important property when the input power is so high, that one should consider the nonlinear propagation regime. A relatively smaller MEA indicates that, for the same optical mode field power, the optical intensity (optical power per unit area) for the mode is higher, leading to a higher nonlinear coefficient. The MEAs as a function of mode p for SIFs and GIFs at 1.55 μm wavelength are plotted in Fig. 1.3(c). As we can see, $A_{\text{eff, mode}\,p}$ for a GIF exhibits an increase with mode number, while for the nondegenerate modes of a SIF, a decrease is observed. Therefore, the lower-order modes of a GIF exhibit a stronger nonlinearity than higher-order modes, which can be beneficial for spatial beam self-cleaning [3, 4].

1.2.2.2 LG mode indexing

The LG modes on the top of Fig. 1.1 can be indexed in terms of a pair of integer numbers (l, m) [5], which indicate their radial and azimuthal properties, respectively. In this way, these modes can be classified by the quantum number q and the azimuthal index m. These indices satisfy the relation $q = 2l + |m|$, where $m = -q, -q+2, \cdots, q-2, q$. An advantage of indexing the modes in this way is that modes with the same quantum number have very similar dispersion properties. For example, in Fig. 1.1(d), the LG modes with the same quantum number have modal effective index $n_{\text{eff},p}$.

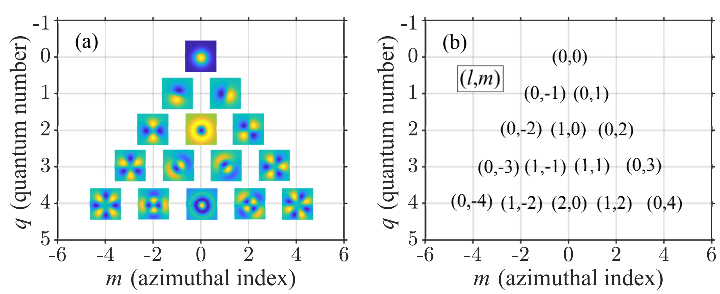

FIGURE 1.2 Mode indexing by quantum number. (a) Illustration of GRIN MMF modes displayed in the (q, m) plane. (b) Relative mapping of the indexes (l, m).

1.2.2.3 Fiber modal dispersion

The second factor that determines fiber features originates from the eigenvalues of the fiber eigenmodes. The eigenvalues are important, because they are directly related to the dispersion properties of the guided modes. In this subsection, we start from the fiber eigenvalues and derive modal dispersion. By comparing different orders of mode dispersion, we show the attractive properties of GIFs when compared with SIFs: higher modal nonlinear coefficients, reduced pulse broadening, and small intermodal walk-off. With these properties, many interesting effects or phenomena are easier to be observed in GIFs, e.g., multimode solitons[6, 7], multimode soliton collisions[8], spatial self imaging[9], and beam self-cleaning[3, 4].

In Fig. 1.1(c,d), we plot the mode eigenvalues as a function of mode order p, for three different wavelengths. The eigenvalues are referred to as modal effective indices $n_p(\lambda)$, which are the numbers quantifying the increase in the wavenumber (phase change per unit length) caused by a waveguide with a finite transverse extension. The modal effective indices decrease when either the mode order p or the wavelength λ increases. This indicates that the confinement of guiding modes with higher order, or at longer wavelengths, becomes weaker.

We can easily obtain the propagation constant $\beta^{(p)}(\lambda)$ of mode p from the modal effective indices as

$$\beta^{(p)}(\lambda) = \frac{2\pi}{\lambda} n_p(\lambda). \tag{1.4}$$

In order to better inspect the physical effects associated with the different orders of modal dispersion, we expand $\beta^{(p)}$ by a Taylor series at the center frequency ω_0 (corresponding to the center wavelength $\lambda_0 = 2\pi c/\omega_0$):

$$\beta^{(p)}(\omega) = \beta_0^{(p)} + \beta_1^{(p)}(\omega-\omega_0) + \frac{1}{2}\beta_2^{(p)}(\omega-\omega_0)^2 + \sum_{n\geq 3}^{\infty} \frac{1}{n!}\beta_n^{(p)}(\omega-\omega_0)^n, \tag{1.5}$$

where

$$\beta_n^{(p)}(\omega) = \frac{\partial^n \beta^{(p)}}{\partial \omega^n}. \tag{1.6}$$

Based on the different orders of dispersion in Eq. (1.6), we highlight the following physical effects or phenomena associated with the individual terms:

(i) Chromatic Dispersion. Chromatic dispersion is the phenomenon whereby the phase velocity and group velocity of light propagating in a medium depend on the optical wavelength (or optical frequency). The terms $\beta_2^{(p)}(\omega)$ are directly related to chromatic dispersion. In Fig. 1.3(b), we plot $\beta_2^{(p)}(\omega)$ as a function of wavelength for the first 15 modes of the GIF. In this figure, there is a wavelength where $\beta_2^{(p)}(\omega) \approx 0$, this occurs at around $1.26\,\mu$m, which is named the zero-dispersion wavelength (ZDW). For this reason, the ZDW is an inflection point for $\beta_1^{(p)}(\omega)$, as can be seen in Fig. 1.3(a). Since the group velocity is inversely proportional to $\beta_1^{(p)}(\omega)$, a light pulse propagates with the fastest speed at this wavelength, when compared with other wavelengths. This is a very important point, because the ZDW separates normal and anomalous dispersion regimes.

In the normal dispersion regime $\lambda < 1.3\,\mu$m, light velocity increases with increasing optical wavelength; whereas in the normal dispersion regime, $\lambda > 1.3\,\mu$m, light velocity decreases with increasing optical wavelength.

In the linear regime, due to the different velocities of the optical frequencies composing a pulse spectrum, a transform-limited Gaussian pulse (unchirped pulse) with duration $T_0 = T_{\mathrm{FWHM}}/1.665$, being T_{FWHM} the full-width at half-maximum, experiences a temporal broadening which is induced by chromatic dispersion. For both anomalous ($\beta_2^{(p)}(\omega) < 0$) and normal dispersion ($\beta_2^{(p)}(\omega) > 0$), the pulse duration increases as $T(z) = T_0\sqrt{1 + (z|\beta_2^{(p)}|/T_0^2)^2}$, where z is the propagation length. The broadening ratio T/T_0 is proportional to $\beta_2^{(p)}$ when $T_0 \ll z|\beta_2^{(p)}|$. In the nonlinear regime, different effects and phenomena are produced in each of the two dispersion regimes.

Chromatic dispersion is slightly different for the different guided modes of s MMF. In Fig. 1.3(f), we plot the values of $\beta_2^{(p)}$ as a function of mode p at $1.55\,\mu$m for GIFs and SIFs. The value of $\beta_2^{(p)}$ for a GIF is much smaller than that for a SIF, as the mode order p grows larger. Therefore, GIFs lead to much smaller pulse broadening ratios among modes, when compared with SIFs.

(ii) Intermodal Dispersion: The group velocity of an optical pulse propagating in a mode of the MMF varies not only with optical frequency (chromatic dispersion), but also with the mode itself. The second term $\beta_1^{(p)}$ in Eq. (1.5) is related to the mode speed via the relation $v_p = 1/\beta_1^{(p)}$. In Fig. 1.3(e), we plot the relative velocity $\Delta v_n = 1/\beta_1^{(p)} - 1/\beta_{1,\mathrm{GRIN}}^{(1)}$ of a mode with index n with respect to the velocity of the fundamental mode $1/\beta_{1,\mathrm{GRIN}}^{(1)}$ of a GIF. As we can see, for a GIF the velocity difference between modes, or intermodal dispersion, is much smaller than for a SIF. Hence, for the same propagation length, the temporal walk-off between modes in GIFs is much smaller than in SIF [see the example in Fig. 1.7 in Sec. 1.4.2].

(iii) Modal Phase: The first term $\beta_0^{(p)}$ in Eq. (1.5) characterizes the phase rotation rate of the field of a given mode during propagation. For example, $\beta_0^{(p)} \approx 6000\,\mathrm{mm}^{-1}$ at $1.55\,\mu$m, which means there are $6000/(2\pi) \approx 955$ periods of rotation per millimeter. In single mode fibers, the effect of the term $\beta_0^{(1)}$ is not significant. However, in MMFs, different modal phase shifts are responsible for multimode interference or mode beating. The most important relation is the phase change difference among the modes of a MMF. In Fig. 1.3(b), we plot the relative value of the phases difference $\delta\beta_0^{(p)} = \beta_0^{(p)} - \beta_{0,\mathrm{STEP}}^{(0)}$, with respect to $\beta_{1,\mathrm{STEP}}^{(0)}$, as a function of mode p for SIFs and GIFs, respectively. For GIF, modes with the same quantum number q have almost identical group velocity and phase change rate. The phase differences among modes with quantum numbers q and $q + 1$ are equally spaced. Therefore, it is easier to observe mode beating in GIFs. If the input pulses are center-coupled into the fiber, only

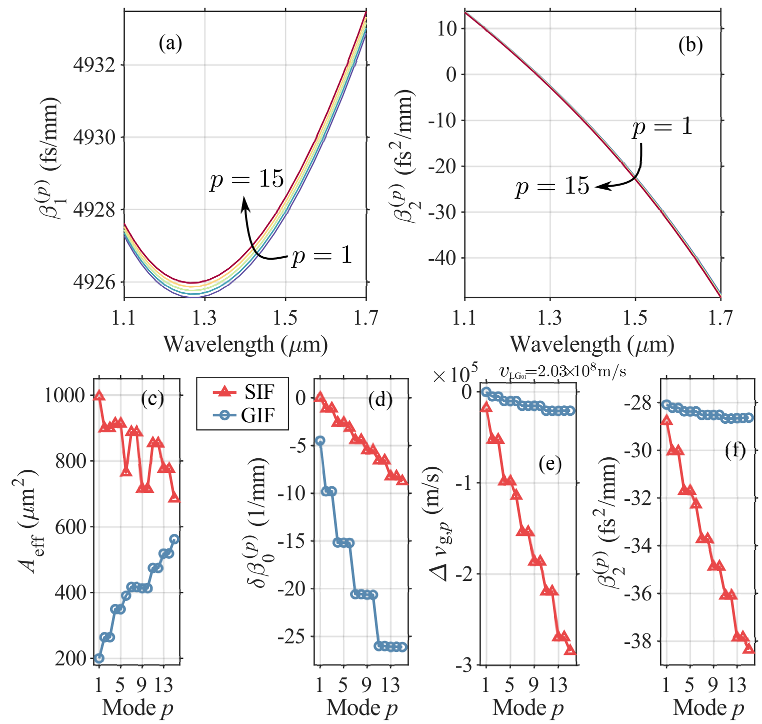

FIGURE 1.3 (a,b) The first $\beta_1^{(p)}$ and second $\beta_2^{(p)}$ order dispersion of the GIF for the first 15 modes, as a function of wavelength λ. (c) Mode effective areas for GIF or SIF in Fig. 1.1. (d-f) Mode dispersion comparison between SIF and GIF with the same core radius of 50 μm at 1.55 μm: (d) relative mode propagation constants $\delta\beta_0^{(p)} = \beta_0^{(p)} - \beta_{0,\text{STEP}}^{(1)}$, (e) relative group velocity $\Delta v_{g,n} = 1/\beta_1^{(p)} - 1/\beta_{1,\text{GRIN}}^{(1)}$, (f) second order dispersion $\beta_2^{(p)}$.

the radially symmetric modes are excited. In this case, because of the reduced modal walk-off, multimode interference is easily observed. As a result, the radial modes of the GIF are periodically in-phase after that they propagate over the distance $L_{\text{SI}} = 2\pi/(\beta_0^{(6)} - \beta_0^{(1)}) = 571.2\,\mu$m [the dispersion values are from Fig. 1.3(d)], periodically leading to beam compression and high intensities at the fiber center. This distance L_{SI}, which is independent of input power, matches well with experimental results [9]. If the input optical power grows above a certain threshold value, the intensities at the points of beam compression are so high that we can directly visualize a periodic array of bright spots, owing to multiphoton absorption activated photo-luminescence [9]. The phenomenon of periodic beam compression is termed spatial self-imaging. However, such high intensities may lead to fiber damage [10, 11]. If asymmetric modes are excited in the GIF, the self-imaging period is doubled to $L_{\text{SI}} = 2\pi/(\beta_0^{(2)} - \beta_0^{(1)})$, and one may even observe plasma self-channeling [4].

Self-imaging in GIFs creates a periodic evolution of the spatial size of the beam, and its intensity. In turn, via the Kerr effect, this leads to a periodic evolution of the effective nonlinearity along the propagation direction. The presence of a periodic nonlinearity may result in the generation series of spectral sidebands, associated with resonant dispersive radiation[12] in the anomalous dispersion regime, and with geometric-type parametric instability (GPI) [13] in the normal dispersion regime. The GPI resonant spectral peaks on both sides of the pump frequency are related to the self-imaging period by the relation $f_h = \pm\sqrt{h}\sqrt{2\pi/(L_{\mathrm{SI}}\beta_2^{(1)})}/2\pi$, where $h = 1,\ 2,\ ,3,\ \cdots$.

1.2.3 Generalized multimode nonlinear Schrödinger equations

Let us consider now nonlinear propagation of optical pulses in a MMF. The optical field can be written as the product of an optical carrier wave $\exp[i(\beta_0^{(0)}z-\omega_0)]$ and a field envelope $\mathcal{E}(x, y, z, t)$, where ω_0 is the optical frequency. $\mathcal{E}(x, y, z, t)$ are normalized such that the field intensity $|\mathcal{E}(x, y, z, t)|^2$ has the units of $\mathrm{W/m^2}$. This field envelope can be expanded on the basis of eigenmodes of MMF as

$$\mathcal{E}(x, y, z, t) = \sum_{p=1}^{N} F_p(x, y)A_p(z, t), \tag{1.7}$$

where $F_p(x, y)$ are the transverse profiles of the modes, as introduced in the previous section. The modes are orthogonal and normalized, so that they obey

$$\int\int F_p(x, y)F_n(x, y)\mathrm{d}x\mathrm{d}y = \delta_{pn}. \tag{1.8}$$

Here, the mode amplitude A_p is expressed in units of $\sqrt{\mathrm{W}}$. The evolution of the field envelope A_p of mode p is governed by the generalized multimode nonlinear Schrödinger equations (GMMNLSEs) [14, 15]:

$$\frac{\partial A_p(z, t)}{\partial z} = \mathcal{D}\{A_p(z, t)\} + \mathcal{N}\{A_p(z, t)\}, \tag{1.9}$$

where the dispersion terms are

$$\mathcal{D} = i(\beta_0^{(p)} - \beta_0^{(1)})A_p - (\beta_1^{(p)} - \beta_1^{(1)})\frac{\partial A_p}{\partial t} + i\sum_{q\geq 2}^{4}\frac{\beta_q^{(p)}}{q!}\left(i\frac{\partial}{\partial t}\right)^q A_p, \tag{1.10}$$

and the nonlinear terms read as

$$\begin{aligned}\mathcal{N} = i\frac{n_2\omega_0}{c}\left(1 + \frac{i}{\omega_0}\frac{\partial}{\partial t}\right)\sum_{l,m,n}^{N}[(1 - f_R)S_{plmn}A_lA_mA_n^* \\ + f_RS_{plmn}A_l\int_{-\infty}^{t}\mathrm{d}\tau h_R * (A_m(z, t-\tau)A_n^*(z, t-\tau))].\end{aligned} \tag{1.11}$$

Here we have supposed that the field, governed by Eqs. (1.9), travels in a reference frame, which has the group velocity of the fundamental mode $1/\beta_1^{(1)}$. Therefore, for all modes, the first two terms in Eq. (1.10) express the relative values of phase group velocity with respect to the fundamental mode. The nonlinear coupling mode coefficients are

$$S_{plmn} = \frac{\int \mathrm{d}x\mathrm{d}y F_p F_l F_m F_n}{\sqrt{\int \mathrm{d}x\mathrm{d}y F_p^2 \int \mathrm{d}x\mathrm{d}y F_l^2 \int \mathrm{d}x\mathrm{d}y F_m^2 \int \mathrm{d}x\mathrm{d}y F_n^2}}. \tag{1.12}$$

For the nonlinear response of the fiber, we consider the standard parameters of silica [16, 17]: the nonlinear index $n_2 = 2.7 \times 10^{-20}\,\mathrm{m^2W^{-1}}$, the coefficient of the Raman contribution to the Kerr effect $f_R = 0.18$. An approximate analytic form is used to describe the Raman response function

$$h_\mathrm{R}(t) = \left(\tau_1^{-2} + \tau_2^{-2}\right)\, \tau_1 \exp(-t/\tau_2)\, \sin(t/\tau_1) \tag{1.13}$$

with two damping time constants $\tau_1 = 12.2$ fs and $\tau_2 = 32$ fs [17].

1.3 CONSERVATIVE SPATIO-TEMPORAL SOLITONS: A VARIATIONAL APPROACH

GIFs with relatively small modal dispersion make it easier to generate multimode solitons. For such fibers, the effect of modal walk-off is not obvious. Within the approximation of neglecting mode walk-off, a simplified model (3D+1) can be used to describe the evolution of electric field $E(x, y, z, t)$ in 3 dimensions (3D) (transverse space (x, y) and propagation direction z) and in one temporal dimension. This model can describe all scenarios where a stable self-imaging pattern is generated in GRIN fibers. The field propagation in a GIF with an instantaneous Kerr nonlinearity is described by a 3D+1 NLSE of the form [18, 9]

$$\frac{\partial E}{\partial z} = \mathrm{i}\frac{1}{2k_0}\left(\frac{\partial^2 E}{\partial x^2} + \frac{\partial^2 E}{\partial y^2}\right) - \mathrm{i}\frac{k_0\Delta}{R^2}(x^2 + y^2)E - \mathrm{i}\frac{\beta_2}{2}\frac{\partial^2 E}{\partial t^2} + \mathrm{i}\frac{k_0 n_2}{n_\mathrm{co}}|E|^2 ECon \tag{1.14}$$

where $k_0 = \omega_0 n_\mathrm{co}/c$ is the wave number, n_co (n_cl) is the refractive index of core (cladding), $\Delta = (n_\mathrm{co}^2 - n_\mathrm{cl}^2)/2n_\mathrm{co}^2$ is the relative refractive index difference, R is the fiber core radius, β_2 is the group velocity dispersion. The 3D+1 NLSE consists of a 1D NLSE, two extra transverse diffraction terms, and a perturbation term given by the inhomogeneous refractive index. The spatial LG modes are eigensolutions of the diffraction and inhomogeneous refractive index terms in Eq. (1.14). When one needs to consider many guided modes, to some extent, this equation can outperform the GMMNLSE in terms of computing efficiency. Moreover, the equation is very similar to the Gross-Piteaevskii equation, which is a well-known model for describing Bose-Einstein condensates. This makes it possible to analogies between two very different physical settings, namely optical and matter waves.

Spatio-temporal solitons, hereafter STS, are coherent light structures which are localized both in time and in space [19]. In principle, they may form whenever material dispersion and diffraction counteract Kerr nonlinearity at once, leading to light confinement in space-time. However, in bulk media, these states may undergo different types of instabilities, such as *spatio-temporal wave collapse* [20, 19], and therefore they are unstable. Different types of stabilization mechanisms have been considered. One of them consists of including explicitly a spatial dependence in the form of a potential, similar to a magnetic trapping potential in the context of BECs [21]. In waveguide systems, this dependence arises naturally in the context of GIFs, and STS stabilization can be achieved.

In this section, we review some of the main results regarding the state of the art of spatio-temporal wave structures, in order to study the formation of STS solitons in conservative multimode GIFs. In order to do so, we apply a variational approach, based on the parameter optimization method. This permits us to compute, analytically, STS solutions starting from a suitable ansatz [22, 23]. For that, we will use the dimensionless version of Eq. (1.14), namely

$$\partial_z u = \frac{i}{2}\nabla_\perp^2 u + i\frac{\delta}{2}\partial_t^2 u + i\frac{s}{2}(x^2+y^2)u + i\nu|u|^2 u, \tag{1.15}$$

where $\nabla_\perp^2 \equiv \partial_x^2 + \partial_y^2$, $\delta = \mathrm{sign}(\beta_2) = \pm 1$ for anomalous/normal dispersion, $\nu = \mathrm{sign}(n_2) = \pm 1$ for self-focusing/self-defocusing nonlinearity, and $s = \mathrm{sign}(\Delta) = \pm 1$ for anti-guiding/guiding materials.

1.3.1 Variational formulation for the 3D+1 inhomogeneous NLS equation

The Lagrangian density corresponding to Eq. (1.15) is given by

$$\mathcal{L} = -\frac{s}{2}\left(x^2+y^2\right)|u|^2 + \frac{\delta}{2}|\partial_t u|^2 - \frac{\nu}{2}|u|^4 + \frac{1}{2}\left(|\partial_x u|^2 + |\partial_y u|^2\right) - \frac{i}{2}\left(u^*\partial_z u - u\partial_z u^*\right),$$

where we have rewritten the derivatives as $u_\xi \equiv \partial_\xi u$, with ξ being any variable x, y, z and t. From this Lagrangian density one can reconstruct the GP Eq. (1.15) by computing the Euler-Lagrange equations

$$\frac{d}{dz}\left(\frac{\partial \mathcal{L}}{\partial u_z^*}\right) + \frac{d}{dt}\left(\frac{\partial \mathcal{L}}{\partial u_t^*}\right) + \frac{d}{dx}\left(\frac{\partial \mathcal{L}}{\partial u_x^*}\right) + \frac{d}{dy}\left(\frac{\partial \mathcal{L}}{\partial u_y^*}\right) - \frac{\partial \mathcal{L}}{\partial u^*} = 0. \tag{1.16}$$

The variational approach consists of four main steps [22, 23]:

- An approximate ansatz solution, or trial function, that captures the main features and shape of the state that we want to compute, is proposed with the form $u = u[x, y, z; p(z)]$, which depends on z through a number of parameters $p(z) = \{p_1(z), \cdots, p_n(z)\}$.
- Next, we calculate the effective Lagrangian function of the system, defined as

$$L(z) \equiv \int \mathcal{L}[u, u_x^2, \cdots]\,dx\,dy\,dt. \tag{1.17}$$

- Subsequently, we compute the Euler-Lagrange equations for each parameter

$$\frac{d}{dz}\left(\frac{\partial L}{\partial(\partial_z p_m)}\right) - \frac{\partial L}{\partial p_m} = 0, \qquad m = 1, \cdots n, \tag{1.18}$$

and study the dynamics of the reduced system.
- Finally, we rebuild the dynamics of the solution by using the ansatz.

1.3.2 The reduced dynamical system for a spatio-temporal soliton

The choice of the approximate solution ansatz is essential for properly capturing the features of the nonlinear solution. The most extended solution ansatz is [24]

$$u(z,x,y,t) = \sqrt{\frac{E\eta(z)}{2\pi a(z)^2}}\operatorname{sech}[t\eta(z)]G(x,y)e^{iC(z,x,y,t)} \tag{1.19}$$

where $G(x, y)$ is a Gaussian function of width $a(z)$

$$G(x,y,z) \equiv \exp\left(-\frac{x^2+y^2}{2a(z)^2}\right),$$

and $C(z, x, y, t)$ is composed by a temporal chirp controlled by $\theta(z)$, a spatial chirp controlled by $\alpha(z)$, and the phase $\phi(z)$, namely

$$C(z,x,y,t) \equiv t^2\theta(z) + \left(x^2+y^2\right)\alpha(z) + \phi(z).$$

The inverse of the temporal width of the sech pulse is $\eta(z)$, and E is the constant pulse energy

$$E = \int\int\int |u(x,y,t)|^2 dxdydt, \tag{1.20}$$

which will be the main control parameter of the STS. The selection of this ansatz in not arbitrary, but it is justified by two main observations:

(a) In the absence of dispersion and nonlinearity, the same equation has Laguerre-Gaussian mode solutions, and the fundamental mode is a Gaussian.
(b) In the absence of diffraction and spatial potential, Eq. (1.15) possesses a sech-shape bright soliton solution in the anomalous GVD regime [19].

With these considerations, the product of a chirped sech pulse and a chirped Gaussian [see Eq. (1.19)] is a reasonable one.

For this solution ansatz, one obtains the effective Lagrangian

$$\begin{aligned} L(z)E^{-1} = \phi'(z) + \frac{\pi^2\theta'}{12\eta^2} + a^2\alpha' + \frac{\delta}{6}\eta^2 + \frac{\pi^2\delta\theta^2}{6\eta^2} \\ - \frac{a^2}{2}(s-4\alpha^2) + \frac{1}{2a^2}\left(1-\frac{\nu E\eta}{6\pi}\right), \end{aligned} \tag{1.21}$$

where $\eta = \eta(z)$, $a = a(z)$, $\theta = \theta(z)$ and $\alpha = \alpha(z)$; derivatives respect to z are $(\cdot)' \equiv \frac{d}{dz}$.

After some simplifications, the Euler-Lagrange equations associated with this effective Lagrangian read

$$\eta'(z) = -2\delta\eta\theta, \tag{1.22a}$$

$$a'(z) = 2a\alpha, \tag{1.22b}$$

$$\theta'(z) = 2\delta\left(\frac{\eta^4}{\pi^2} - \theta^2\right) - \frac{E\nu\eta^3}{2\pi^3 a^2}, \tag{1.22c}$$

$$\alpha'(z) = \frac{1}{2a^4}\left(1 - \frac{\nu\eta E}{6\pi}\right) + \frac{s}{2} - 2\alpha^2. \tag{1.22d}$$

With this approach we have been able to reduce the infinite dimensional Eq. (1.15) to a 4D dynamical system, describing the variation of the four parameters describing the adiabatic evolution of the soliton ansatz along the propagation distance.

1.3.3 General fixed points solutions

Here we are interested in the steady, or shape preserving, states of Eq. (1.15), which correspond to the fixed or equilibrium points of the effective reduced system (1.22). Equilibria $(\eta, a, \theta, \alpha) = (\eta_e, a_e, \theta_e, \alpha_e)$ of Eqs. (1.22) satisfy the condition $[\eta'(z), a'(z), \theta'(z), \alpha'(z)] = [0, 0, 0, 0]$.

There are two main equilibria, which are both chirp-free. The simplest one corresponds to the continuous wave (CW) beam and reads as

$$\eta_e = 0, \qquad a_e = 1, \qquad \theta_e = 0, \qquad \alpha_e = 0. \tag{1.23}$$

The other solution corresponds to an STS, satisfying the condition

$$a_e^2 = \frac{E\nu}{4\pi\delta\eta_e}, \qquad \frac{3sE^2}{8\pi} - E\nu\eta_e^3 + 6\pi\eta_e^2 = 0, \qquad \theta_e = 0, \qquad \alpha_e = 0. \tag{1.24}$$

The second equation can be solved for E, so that the following expression is obtained

$$E = \frac{4\pi}{3s}\eta_e\left(\nu\eta_e^2 \pm \sqrt{\eta_e^4 - 9s}\right). \tag{1.25}$$

The stability of the fixed points can be evaluated by solving the linear eigenvalue problem $\mathcal{J}w = \lambda w$, where λ and w are the eigenvalue and eigenvector associated with the Jacobian of the dynamical system (1.22), respectively. This can be done analytically, although the expressions obtained are not easily tractable. Here we will numerically compute the stability by means of the path-continuation software package AUTO-07p [25, 26].

In what follows, we will show some of the most relevant results for two different scenarios where Eq. (1.25) has a physical meaning:

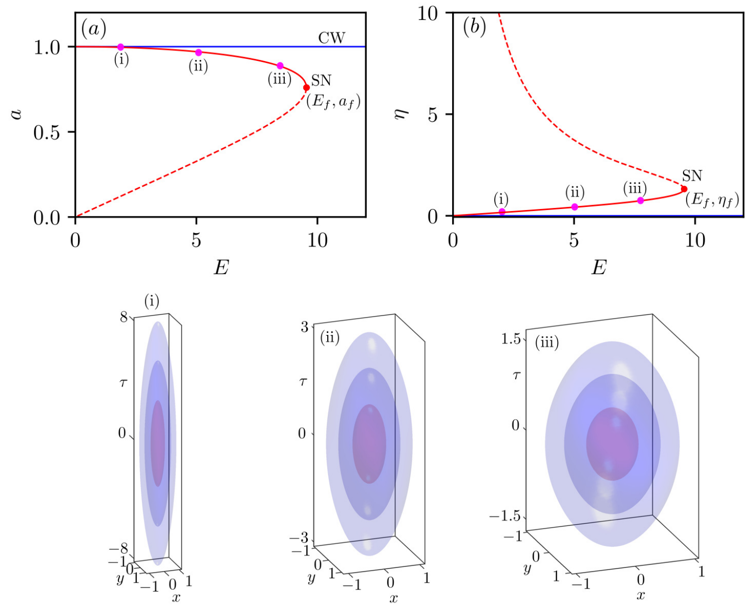

FIGURE 1.4 Bifurcation diagrams and LBs for a guiding ($s = -1$), self-focusing material ($\nu = 1$) with anomalous GVD ($\delta = 1$). (a) Spatial width of the LB as function of E in blue and CW in red. (b) shows the inverse of the temporal width η of the LB as a function of E (in blue) and the CW state in red. Solid (dashed) lines stand for stable (unstable) states. Some examples of stable LBs are shown in panels (i)-(iii) for energies $E = 2, 5$, and 8, respectively. To represent them we plot 3 isosurfaces for different intensities.

- Guiding, self-focusing material with anomalous GVD ($s = -1, \nu = \delta = 1$);
- Guiding, self-defocusing material with normal GVD ($s = \nu = \delta = -1$).

1.3.4 Guiding, self-focusing material with anomalous GVD

The first scenario presented here was first reported by Yu *et al.* in 1995 [27], although by using a different ansatz than ours. This scenario focuses on inhomogeneous media with self-focusing ($\nu = 1$) and guiding ($s = -1$) potentials in the anomalous GVD ($\delta = 1$) regime; the equilibrium point corresponding to the STS becomes

$$a_e^2 = \frac{E}{4\pi\eta_e}, \qquad E = \frac{4\pi}{3}\eta_e\left(\sqrt{\eta_e^4 + 9} - \eta_e^2\right). \tag{1.26}$$

The spatial width a_e and the inverse of the temporal width η_e of the STS with energy E are shown in the bifurcation diagram plotted in Fig. 1.4(a) and Fig. 1.4(b), respectively.

The stable STS emerges from the CW state at $E = 0$ [see Figs. 1.4(a,b)]. The spatial width decreases with E from $a_e = 1$ until $a_e = a_f$, where a fold or saddle-node bifurcation [28] occurs at $E = E_f$. At this point, the STS becomes unstable (see dashed line), and the solution curve folds back to lower values of E. With decreasing E, a_e decreases and asymptotically approaches $a = 0$. The fold at (E_f, a_f) defines the upper region of existence of the STSs. Above it, STS solutions do not exist, and the only attractor is the CW beam state.

The fold position can be calculated analytically, by solving the equation $dE/d\eta_e = 0$. This leads to the values

$$\eta_f = 3^{1/4}, \qquad E_f = \frac{4\pi}{3^{3/4}}(\sqrt{12} - \sqrt{3}), \qquad a_e = \sqrt{\frac{\sqrt{12} - \sqrt{3}}{3}}. \tag{1.27}$$

The modification of the STS states along the stable branch is shown in Fig. 1.4(i)-(iii) for $E = 2, 5$ and 8, respectively.

The modification of η_e with E is plotted in Fig. 1.4(b). By increasing E, η_e increases, while its inverse (i.e., the temporal width) decreases. This tendency can be easily observed in the STSs shape shown in Figs. 1.4(i)-(iii): for very small E, the STS is almost a cylinder, which decreases its temporal width while increasing E. These states have been reconstructed from the ansatz (1.19). Once the fold is passed, the STS decreases both its temporal (η_e^{-1}) and spatial widths (a_e), and eventually becomes a spatio-temporal singularity for $E \to 0$.

1.3.5 Guiding, self-defocusing material with normal GVD: Neutral STSs and periodic oscillations

Now we consider a guiding ($s = -1$) and self-defocusing ($\nu = -1$) multimode fiber with normal GVD ($\delta = -1$). This scenario was first analyzed by Raghavan and Agrawal in 2000 [24].

The STS equilibrium solution of the system reduces to

$$a_e^2 = \frac{E}{4\pi\eta_e}, \qquad E = \frac{4\pi}{3}\eta_e\left(\eta_e^2 + \sqrt{\eta_e^4 + 9}\right). \tag{1.28}$$

The dependence of the a_e and η_e parameters with E is plotted in Figs. 1.5 (a) and (b). This STS bifurcates from the CW beam state (see red line). Figure 1.5(a) shows how the STS spatial width a_e grows with E, as so does η_e (its temporal width η_e^{-1} decreases) [see Fig. 1.5 (b)]. Here, in contrast to the scenario presented in Sec. 1.3.4, the STS does not undergo any fold bifurcation, and it exists for any value of E.

For low values of E, the linearization of the system (1.22) around the STS fixed point parameters leads to the pure complex eigenvalues

$$\lambda_{1,2} = \pm i\sqrt{\left(4 + \frac{E^2}{2\pi^2}\right)} \equiv \pm iK_1, \qquad \lambda = \pm i\frac{E^2}{4\sqrt{2}\pi^3} \equiv \pm iK_2. \tag{1.29}$$

A fixed point with these eigenvalues is a *center* equilibrium [28]. Center points are neutrally stable, in the sense that nearby trajectories (i.e., soliton parameter

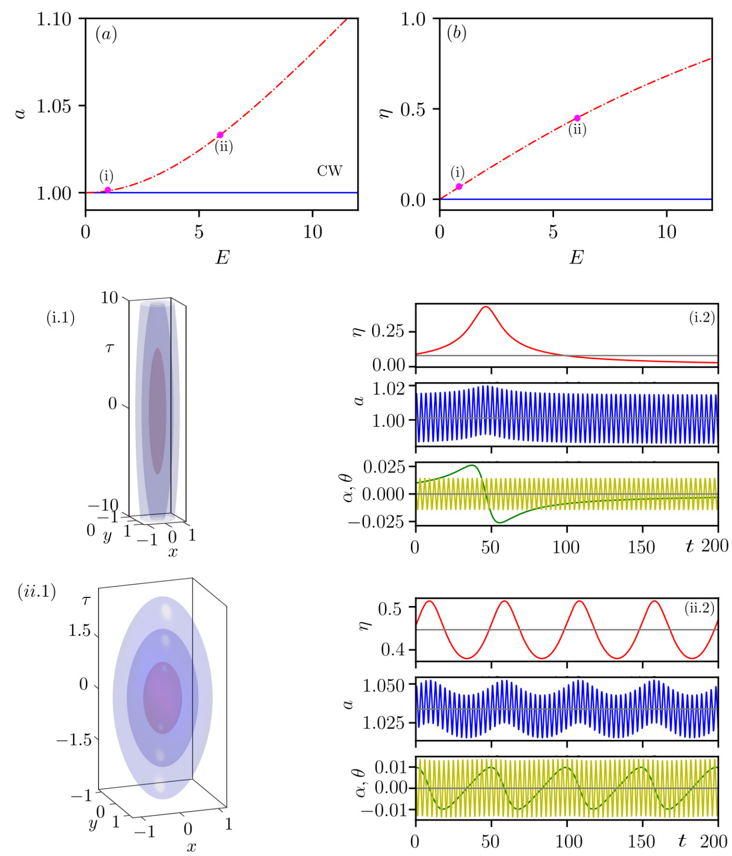

FIGURE 1.5 (a) Spatial width a of the shape-preserving states of Eq. (1.22), plotted as a function of E. In blue we show the CW beam, and in point-dashed red the neutrally stable STS. (b) Inverse of the temporal width η of the shape preserving states as a function of E. In both diagrams, the label (i) corresponds to the neutrally stable STS center shown in Fig. 1.5(i.1) for $E = 1$. The gray lines show the evolution of the unperturbed STS. Panels (ii.1) and (ii.2) show the unperturbed STS center $(\eta_e, a_e) = (0.4467, 1.034)$, and periodic oscillations for $E = 6$.

perturbations) are neither repelled nor attracted to it, but they undergo permanent oscillations. Neutral instability is depicted by using red point-dashed lines in Figs. 1.5(a) and (b).

An STS center is plotted in Fig. 1.5(i.1) for $E = 1$ [see (i) in Fig. 1.5(a),(b)]. Figure 1.5(i.2) shows in gray the constant temporal evolution of such unperturbed state. The temporal evolution of a perturbed STS center is shown in Fig. 1.5(i.2) for a constant homogeneous perturbation factor 0.01. This perturbation leads to periodic oscillations with two different frequencies: a and α oscillate with a higher frequency, while η (red line) and θ (green line) with a lower one. In the phase space, these oscillations correspond to closed orbits. However, in contrast to limit cycles, these orbits are not isolated, but form a continuous family around the center point [24]. In this sense, different perturbations lead to different oscillatory STS, which coexist for the same energy.

By increasing the energy E, the STS center and the periodic oscillations modify in shape, amplitude and periodicity, respectively. For $E = 6$ [see (ii) in Fig. 1.5], the STS center is depicted in Fig. 1.5(ii.1). The periodic oscillations emerging from perturbing such state with a homogeneous and constant factor 0.01 are shown Fig. 1.5(ii.2). For this value of energy, a and α oscillate at a frequency very similar to the case for $E = 1$, while oscillations of η and η have increased their frequency.

1.4 STABLE SOLUTIONS OF THE NONLINEAR EQUATIONS

1.4.1 Single-mode solution

The generalized nonlinear Schrödinger equation (1.9) can be simplified in the case of a single-mode fiber, such as the standard monomodal fiber (SMF) or the dispersion-shifted fiber (DS) [29], which can only transmit the fundamental mode; we consider here the propagation effects caused by GVD, or second-order chromatic dispersion β_2 (s^2/m), and by Kerr nonlinearity, represented by the nonlinear coefficient $\gamma = 2\pi n_2/\lambda A_{eff}$ ($W^{-1}m^{-1}$), where A_{eff} and λ are the effective area of the fundamental mode and the field carrier wavelength, respectively; we also consider fiber linear losses, represented by the loss coefficient α (m^{-1}). Hence, Eq. (1.9) reduces to [17]

$$\frac{\partial A(z,t)}{\partial z} = -i\frac{\beta_2}{2}\frac{\partial^2 A}{\partial t^2} + i\gamma|A^2|A - \frac{\alpha}{2}A, \tag{1.30}$$

where $A(z,t)$ is the field's complex amplitude ($\sqrt{W}$), describing the evolution, with distance z, of the temporal shape of a propagating optical signal. We now consider the transmission of an optical pulse with temporal pulsewidth T_0, and introduce the dispersion length $L_D = T_0^2/|\beta_2|$, defined as the fiber distance where chromatic dispersion causes an increase of the optical pulse duration by a factor $\sqrt{2}$, and the nonlinear length $L_{NL} = \lambda T_0 w_e^2/(n_2 E_p)$, which is the fiber distance where the nonlinear effects start affecting field propagation, being w_e and E_p the beam waist in the fiber and the pulse energy, respectively. In a single-mode fiber, the beam waist approximates the fiber radius (generally, 4 to 5 μm). We also introduce the parameter N as

$$N^2 = \frac{L_D}{L_{NL}} = \frac{n_2 E_p T_0}{\lambda|\beta_2|w_e^2}. \tag{1.31}$$

For $N >> 1$, nonlinear effects prevail over dispersive effects; conversely, for $N << 1$, the dispersive effects are dominant. By solving Eq. (1.30) using the inverse scattering method [30][31], it is possible to demonstrate that a stable solution exists for negligible losses, anomalous fiber dispersion ($\beta_2 < 0$), whenever dispersive and nonlinear effects compensate for each other, hence, for $N = 1$; the solution is the single-mode fundamental soliton, whose temporal shape is conserved with distance, and is given by

$$A(z,t) = \sqrt{P_0}\,\mathrm{sech}\left(\frac{t}{T_0}\right)\exp\left(i\frac{z}{2L_D}\right), \tag{1.32}$$

with $P_0 = E_p/(2T_0)$ the pulse peak power, and the constant full-width half-maximum pulsewidth is given by $T_{FWHM} = 1.763 \cdot T_0$. The condition $N = 1$ provides a specific energy for the soliton pulse, which is related to the pulsewidth T_0 by the relationship

$$E_s = \frac{\lambda|\beta_2(\lambda)|w_e^2}{n_2 T_0}. \tag{1.33}$$

An optical pulse entering the fiber with energy and pulsewidth related by Eq. (1.33), spontaneously evolves into a sech temporal shape, and propagates unperturbed over potentially unlimited distances; both pulsewidth and spectral width will remain unchanged; hence, this type of optical pulse has attracted large attention in telecom applications [32][33]. The transverse beam profile is substantially unperturbed as well, exhibiting the well-known Gaussian profile of a fundamental fiber mode. In the presence of fiber losses, which are generally compensated for at every fiber distance L_A by all-optical amplifiers with power gain G, a stable solution is still possible for the perturbed equation (1.30), provided that the pulse power at the output of each amplifier equals

$$P_s = \frac{G\ln G}{G-1}P_0, \tag{1.34}$$

and the amplifier spacing $L_A << L_D$ [34].

1.4.2 Multimode solution

In multimode fibers, the propagation of optical signals can be described by the 3D+1 nonlinear Schrödinger equation, Eq. (1.15), or by the coupled equation model, or GMMNLSE, Eq. (1.9). In GIFs with a parabolic index profile, the trial function of Eq. (1.19) provides an approximate solution of the 3D+1 equation, under the variational approximation [35][36]. If the optical transverse field injected into the fiber is a Gaussian beam, in the weakly or moderate nonlinear regime, the propagating transverse field is still approximately Gaussian, and the beam waist $w(z)$ periodically oscillates with distance; the periodical evolution of the beam is caused by the interference between modes with equally spaced propagation constants (see 1.2.2.3). The absolute value of the total field can expressed as

$$|E(x,y,z,t)| = E_0(z,t)\frac{w_{in}}{w(z)}\exp\left[-\frac{x^2+y^2}{w^2(z)}\right], \tag{1.35}$$

and the beam waist varies with respect to the input value w_{in} according to the relation [37][38]

$$\frac{w(z)}{w_{in}} = \left[\cos^2(\pi\frac{z}{z_p}) + C^2\sin^2(\pi\frac{z}{z_p})\right]^{1/2}, \tag{1.36}$$

where $z_p = \pi r_c/\sqrt{2\Delta}$ is the beam waist oscillation period, r_c the radius of the fiber core, $\Delta = (n_{co}^2 - n_{cl}^2)/2n_{co}^2$ the relative index difference between the core and the cladding, and $C = \lambda z_p/n_{co}\pi^2 w_{in}^2$ is a measure of the oscillation amplitude. The oscillation of the beam waist in a GIF is commonly referred to as self-imaging [9], an effect observed also in the non-soliton, or linear regime.

Figure 1.6 shows an example for the spatial evolution of the beam effective area in a GIF, at the telecom wavelength of 1550 nm; the area was calculated from Eq. (1.3), after simulating the beam propagation with the 3D+1 model of Eq. (1.15). The fiber parameters of the simulation are: β_2=-28.7 ps^2/km, n_2=2.7x10^{-20} m^2/W, n_{cl}=1.444, Δ=0.0103, r_c=25 μm. The effective area is related to the beam waist by the approximate expression $A_{eff} = \pi w^2(z)$. Several input beam waist values were tested: for w_{in}=7.8 μm, the self-imaging amplitude $C = 1$, and no beam waist oscillation is observed; this case corresponds to the excitation and propagation of the fundamental mode. For smaller values (w_{in}=4.5 μm in the figure), the beam periodically expands with respect to the input transverse dimension; for larger values (w_{in}=9.5 and 15 μm in the figure), the beam periodically compresses to a minimum value; the effective area can be greatly reduced with respect to the input value, thus increasing the intensity by a factor C. The oscillation period for the effective area is constant with the input waist: typically, it is of the order of 0.55 mm at telecom wavelengths.

In multimode SIFs, the self-imaging effect is not observed, because different modes have propagation constants with non-uniform spacing (see section 1.2.2.3).

If the total energy of the optical pulse is much smaller than the soliton threshold given by Eq. 1.33, the temporal profile of an optical pulse propagating in a GIF, or in a SIF, is strongly affected by the modal dispersion. Fig. 1.7 provides an example, obtained by using the model introduced in Sec. 1.2.3, of an ultra-short optical pulse propagation in (a) a GIF, and (b) a SIF. The pulse is initially composed by the first three radial modes [see mode $p = 1, 6, 15$ in Fig. 1.1], with the energy ratio $R_{\mathrm{M}} = 0.48 : 0.32 : 0.21$ at the center wavelength $\lambda_{\mathrm{c}} = 1550$ nm. The fiber length is 1 m, and the pulse energy (2 pJ) is sufficiently small to experience negligible Kerr and Raman nonlinearities; hence, the pulse propagates in the linear regime. The energies E_1, E_2 and E_3 for the three modes at each fiber position are given on the right side of each sub-figure.

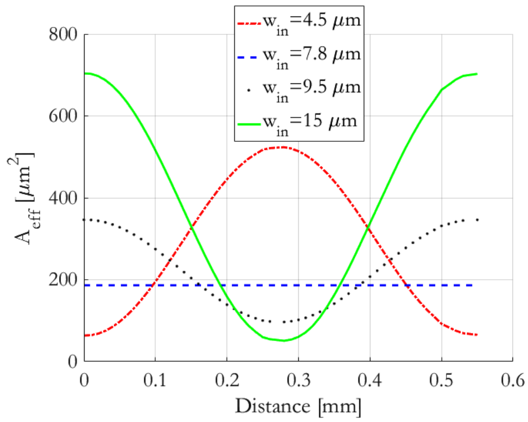

FIGURE 1.6 Evolution of the beam's effective area in a GRIN fiber, for different values of the input beam waist.

In fig. 1.7(a), the effect of modal dispersion is visible as it leads to a gradual separation of optical pulses corresponding to each of the different modes (the red, green, and blue curves); also, the pulse duration of three modes gradually increases, owing to chromatic dispersion β_2. As a result, the three modes broaden in time, and start to walk-off in time, each with its own modal group velocity $1/\beta_1^{(n)}$; the fundamental mode has a higher velocity with respect to the other modes [see Fig. 1.3(e)], which as a result appear to be delayed in time.

In Fig. 1.7(b), the pulse evolution in a SIF is reported, with the same input conditions as in the GIF. The pulse duration of the three modes grows larger as a consequence of chromatic dispersion, as it occurs for a GIF, but the mode pulse delay owing to modal dispersion is considerably larger than in the case of the GIF. Specifically, one can analytically verify the pulse delay between two modes by calculating the walk-off time $\tau_\mathrm{d} \approx L(v_{\mathrm{LP}_{01}} - \Delta v)^{-1} - Lv_{\mathrm{LP}_{01}}^{-1} \approx L\Delta v/v_{\mathrm{LP}_{01}}^2$, where Δv is the velocity difference between two modes. For example, the delay time $\tau_d = L\Delta v/v_{\mathrm{LP}_{01}}^2 = 6.55$ ps between mode 1 and mode 15 for the SIF at $L = 1$ m, with the parameters in Fig. 1.3(d) ($\Delta v = 2.7 \times 10^5$ m/s, $v_{\mathrm{LP}_{01}} = 2.03 \times 10^5$ m/s).

When pulses propagate in a GIF with anomalous dispersion, and the (total) energy of the optical pulse is increased up to the soliton value, given by Eq. 1.33 with w_e the effective waist of the multimode beam, the Kerr nonlinearity produces an instantaneous optical self-phase-modulation, or relative frequency shift between the trailing and leading edges of a pulse. The central wavelength of pulses corresponding to the higher-order modes is reduced by the Kerr nonlinearity; the wavelength of lower-order modes is increased; hence, anomalous chromatic dispersion accelerates the higher order modes and slow-down the lower-order ones, compensating the delay produced by the modal dispersion. As a result, both the temporal broadening of pulses within individual modes,

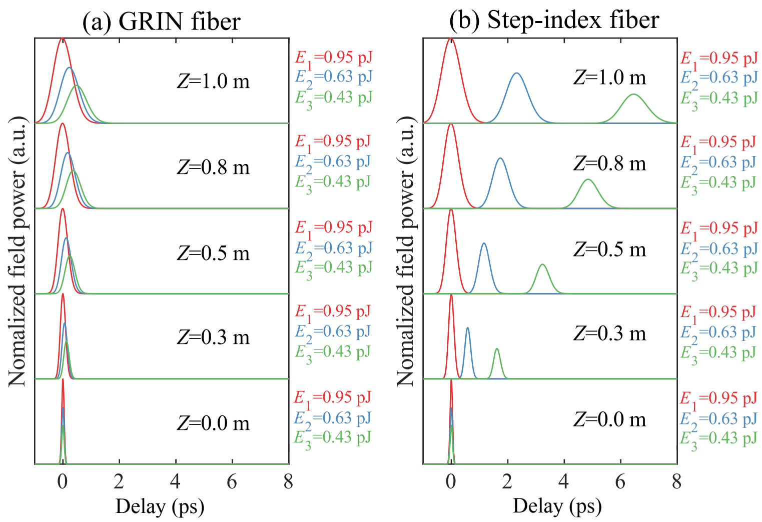

FIGURE 1.7 Comparison of temporal power evolution of a multimode pulse in (a) GIF and (b) SIF, when the input pulse energy is 2 pJ. The modes are plotted by a red line (mode $p = 1$), a blue line (mode $p = 6$) and a green line (mode $p = 15$), respectively. The fiber length is $L = 1$ m. The initial mode energy ratio is $0.48 : 0.32 : 0.21$.

induced by the chromatic dispersion, and their relative time delay induced by the modal dispersion, are balanced by the fiber nonlinearity. Optical pulses, corresponding to different modes, trap each other in the time domain, and propagate with the same velocity, without any temporal broadening. Both the temporal profile $A(z,t)$ of the multimode soliton, and its spectral profile, assume a sech shape, just as in the single mode case; the pulsewidth and the spectral width remain unchanged, in spite of the periodical oscillations on the transverse field. In other words, the pulse intensity $|E(x, y, z, t)|^2$ undergoes periodical oscillations, with period z_p; the pulse power, to the contrary, maintains unchanged its temporal profile $|A(z,t)|^2 = (\pi w_{in}^2/2)|E_0(z,t)|^2 = P_0 \,\mathrm{sech}^2(t/T_0)$, with P_0 the pulse peak power, in W.

Multimode soliton propagation, as described by the variational approach [39] only holds over short spans (a few meters) of GIF. Experimental evidence, shown in the next section, confirms that multimode solitons spontaneously converge into a fundamental single-mode soliton over large distances but, unlike the case of single-mode fiber solutions, they possess specific values of pulsewidth and energy, which remain stable over long-range propagation distances.

1.4.3 The multimode walk-off soliton

Whenever a multimode soliton propagates over long spans of GIF (i.e., longer than 100 m), its behavior differs from what is predicted by the variational theory described in sections 1.3 and 1.4.2. Fig. 1.8 illustrates a numerical simulation carried out by using the coupled-mode equations model, Eq. 1.9. An optical pulse with T_{FWHM}=235 fs is coupled at the input of the fiber, with energy distributed over the first 3 modes with axial symmetry, e.g., the Laguerre-Gauss modes with radial/azimuthal indexes $(p, m) = (0, 0), (1, 0), (2, 0)$; the power distributed among non-axial modes can be neglected at the fiber input. The pulse propagates over 120 m of fiber, at 1550 nm wavelength, with energy E_p=2.5 nJ [7].

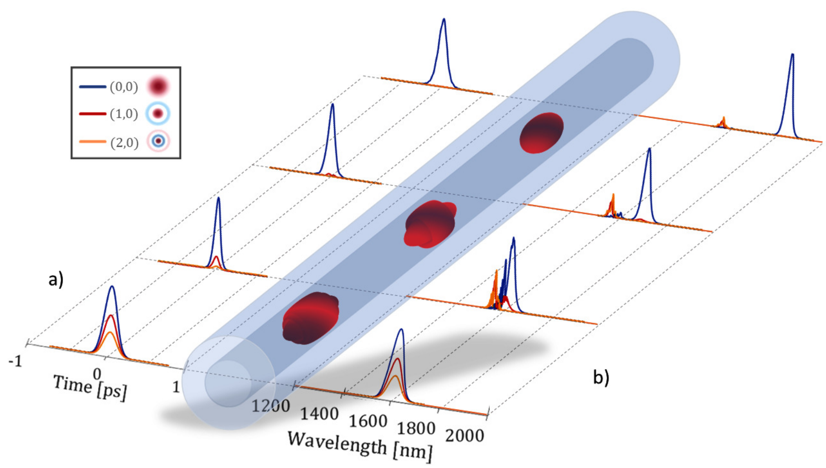

FIGURE 1.8 Multimode soliton formed from an input 235 fs pulse, composed by 3 axial modes, propagating over 120 m of GIF, at the optimal input energy of 2.5 nJ. a): mode powers, b): mode spectra (From Ref. [7]).

The nonlinear coupling coefficients S_{plmn} in Eq. 1.11, are responsible for inter-modal four-wave mixing (IM-FWM) and inter-modal stimulated Raman scattering (IM-SRS) [40]; they produce, in the time domain (see Fig 1.8a), a slow transfer of energy towards the fundamental mode $(0, 0)$. Whereas in the frequency domain (see Fig. 1.8b) a red-shift of the pulse wavelength occurs: this is commonly referred to as Raman-induced soliton self-frequency shift (SSFS) [41][42][43].

As a result, the propagating bullet converges to a field with Gaussian transverse profile, which is typical of the fundamental mode, and with sech-shaped temporal profile [6]. The distance required to complete the process is of the order of 100 m, corresponding to hundreds of nonlinear lengths L_{NL}. Hence, the self-imaging effect of the beam waist vanishes after tens of meters of fiber, when the fundamental mode has collected most of the pulse energy, at the expense of higher-order modes. The effective waist of the propagating beam can be taken as the mean value of Eq. 1.36, which is equal to

$$w_e = w_{in}\sqrt{(1+C^2)/2}; \tag{1.37}$$

After tens of meters, the effective beam waist gradually reduces to the waist of the fundamental mode, which can be calculated from the condition $C = 1$ as

$$w_0 = \sqrt{\lambda r_c/(\pi n_{co}\sqrt{2\Delta})}. \tag{1.38}$$

A second peculiar property of multimode solitons is their pulsewidth invariance with respect to the input pulse duration. Fig. 1.9 shows a numerical simulation of pulses propagating over 10 m of GIF; the tested input pulse durations are 67 fs or 235 fs, respectively; input wavelengths are 1350 nm, 1550 nm, and 1680 nm. The input excitation involves the axial-symmetric $(0,0)$, $(1,0)$, $(2,0)$ modes. In all cases, an optimal input pulse energy is chosen in order to provide the minimum pulsewidth after 1 km of fiber; hence, the pulse energy is selected to observe the highest pulse stability at large distances. The optimal value of the pulse energy ranges between 1.5 and 3 nJ, depending on the input wavelength. For each tested wavelength, both pulses with input pulsewidth of 67 fs and 235 fs form, after 2 m propagation, a multimode soliton with the same pulsewidth. In the figure, solitons propagate up to 10 m, experiencing a spectral red-shift induced by Raman SSFS. The soliton condition given by Eq. 1.33 still holds for short-distance multimode solitons; according to that equation, because of the increase of both the soliton wavelength and the absolute value of the GVD, the pulse duration must increase with distance, in order to preserve the soliton condition.

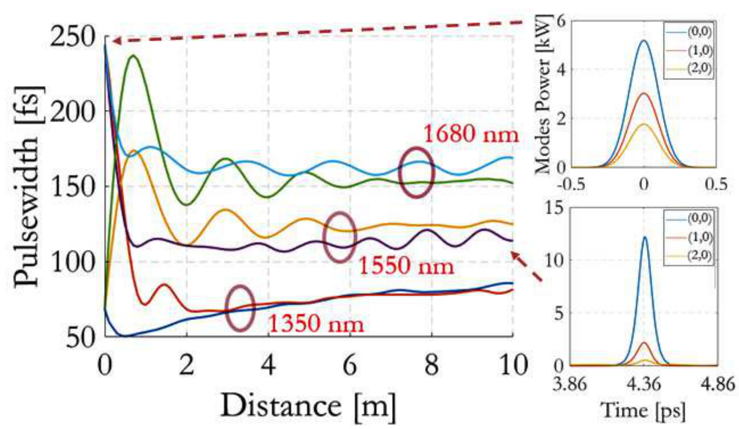

FIGURE 1.9 Simulated soliton pulse widths for input pulses of 67 fs and 235 fs duration, and input wavelengths of 1350 nm, 1550 nm, 1680 nm, respectively. The input modes are (0,0), (1,0), (2,0). Right insets: modal powers at the fiber input (top), and after 10 m of propagation (bottom), for 1550 nm input wavelength and 235 fs input pulsewidth. From Ref. [7].

The right insets in Fig. 1.9 show the modal powers at the fiber input (top), and after 10 m of propagation (bottom), for the case of 1550 nm input wavelength and 235 fs input pulsewidth; the walk-off soliton formed after a few meters has 120 fs pulsewidth. After 10 m of distance, most of its energy is transferred into the fundamental mode; the same soliton pulse duration is obtained from a 67 fs input pulse. Finally, from Fig. 1.9 it is clear how the pulse duration T_s of the soliton, immediately after its formation, is independent on input pulse duration, but it increases with the input wavelength: after 2 m, it acquires the values of 70, 120, and 160 fs for input wavelengths of 1350, 1550, 1580 nm, respectively. The energy of soliton formation is provided by Eq. 1.33, after replacing $T_0 = T_s/1.763$, and the effective beam waist w_e from Eq. 1.37.

An explanation for the pulsewidth invariance of multimode solitons can be provided by introducing the walk-off length

$$L_W = T_0/\overline{\Delta\beta_1}, \tag{1.39}$$

where $\overline{\Delta\beta_1} = \sum f_n[\beta_{1n}(\lambda) - \beta_{11}(\lambda)]/\sum f_n$ is the weighted mean of the modal group velocities $\beta_{1n}(\lambda)$ (s/m) relative to the fundamental mode, $n = 1, 2, \ldots N$ is a mode index, N the number of modes, and f_n the fraction of pulse energy carried by the mode n. The modal walk-off length is the distance where pulses carrying individual modes separate in time, because of modal dispersion. We also introduce the random mode coupling and birefringence correlation lengths, L_{cm} and L_{cp}, which are the characteristic length scales associated with linear coupling between degenerate modes or between polarizations, respectively [44][45][46][47]. The generation of a multimode soliton, including non-degenerate modes, is only possible providing that nonlinearity acts over distances which are shorter than those associated with random mode coupling and birefringence, i.e., for $L_{NL} < L_{cm}, L_{cp}$. A second requirement to be considered is that both the dispersion and nonlinearity lengths are of the same order of the modal walk-off length

$$L_D = L_{NL} = const \cdot L_W, \tag{1.40}$$

where $const$ is an adjustment constant. A similar condition for the nonlinearity-induced temporal trapping of optical fiber modes was initially predicted, for the j-th mode, by [48][49] as $L_{Wj} \geq L_D = L_{NL}$. Based on the above considerations, by replacing into Eq. 1.40 the expressions for the dispersion, nonlinearity and walk-off lengths, we can find the condition to be respected by the multimode 'walk-off' soliton pulsewidth at the distance of initial formation [7].

$$T_s(\lambda) = const \cdot 1.763 \frac{|\beta_2(\lambda)|}{\overline{\Delta\beta_1}(\lambda)}. \tag{1.41}$$

In Eq. 1.41, there is no dependence of the soliton pulsewidth on the input pulse duration. Conversely, the soliton pulsewidth depends on the fiber dispersion parameters, which are wavelength dependent. The adjustment constant const depends on the coupling condition of the beam at the fiber input, and it is generally close to unity.

Fig. 1.10 provides a comparison of experimental data with the theory of multimode walk-off solitons. It provides the measured pulsewidth, after 6 m or after 830 m of GRIN fiber, respectively, vs. the soliton energy. Input wavelength and pulsewidth used in this experiment are: 1450 nm and 60 fs, 1550 nm and 70 fs, 1650 nm and 60 fs, respectively; the beam diameter at the fiber input is approximately 30 μm (w_{in}=15 μm) [50]. The experimental curves after 830 m of fiber confirm the existence of an optimal pulse energy, which provides a minimum long-distance pulsewidth. Whereas the soliton energy increases with wavelength (1.0, 1.5, 2.2 nJ at 1450, 1550, 1650 nm, respectively). Such an effect is not visible at short distances (6 m), where the pulsewidth of the forming soliton scales with the energy according to the theory of Eq. 1.33, providing that an effective waist w_e=9.5 μm is used, close to the fundamental mode waist of 7.8 μm. The only visible difference from the short-distance pulsewidth, with respect to the theory, is a small local increase of the pulse duration, which occurs immediately above the value of optimal energy for long-distance soliton formation.

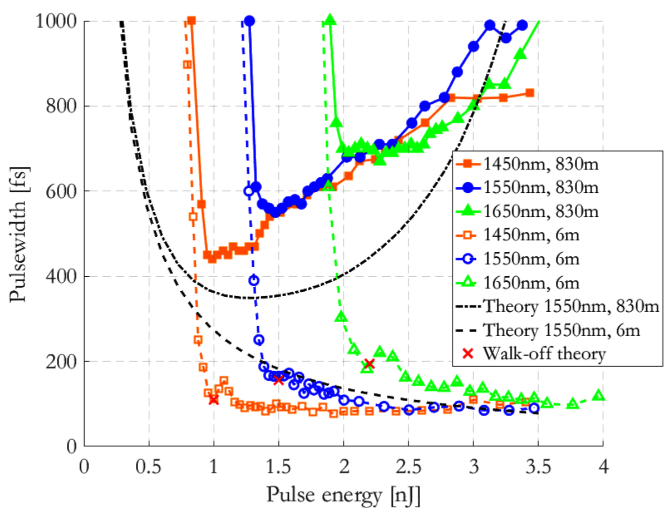

FIGURE 1.10 Experimental pulsewidth vs. soliton energy for a pulse propagating over 6 m or 830 m of GRIN fiber. Input parameters are: 1450 nm and 60 fs, 1550 nm and 70 fs, 1650 nm and 60 fs; 30 μm beam diameter. Theoretical curves are calculated from Eq. 1.33. Red x-crosses come from Eq. 1.41. From Ref. [50].

In Fig. 1.10, theoretical curves at 1550 nm, and at distances of 6 m or 830 m, respectively, are calculated from Eq. (1.33). Here we also account for the Raman-induced red-shift, and wavelength-dependent dispersion; pulse energy reduction, due to fiber losses, was also accounted for when using the equation.

At relatively short distances, the theory provides a fairly good agreement with experimental data, at all tested input energies. Whereas at long distances, the wavelength-dependent losses are partially responsible, together with the Raman-induced wavelength red-shift, for the output pulsewidth increase which is observed for input pulse energies above the optimal value. From the comparison of theoretical curves with experiments, it is found that the curve obtained from Eq. (1.33), which is derived from the single-mode soliton theory, does not correctly reproduce the experimental data for describing long-distance multimode solitons.

On the other hand, the walk-off soliton theory of Eq. (1.41) is able to predict well the pulsewidth of the MM soliton that is formed at short distances. Starting from the measured soliton wavelengths of 1487, 1586, 1672 nm at 6 m of distance, with the optimal energies of 1.0, 1.5, 2.2 nJ, for input wavelengths 1450, 1550, 1650 nm, respectively, using GIF dispersion curves, and choosing an adjustment constant *const*=1.0, the calculated solitons pulsewidth are 112, 158, 198 fs, respectively. The corresponding three points are indicated by red x-crosses in Fig. 1.10, and show an excellent agreement with experimental data.

When considering multimode soliton formation in SIFs, experimental evidence [51] shows that for SIF solitons, similar conditions to the case of GIFs still hold; hence, the same invariance of the initial pulsewidth is found, and the MM soliton tends to converge to a single-mode soliton. The basic difference is that a SIF soliton only forms among the first 3 modes $LP_{01}, LP_{11a}, LP_{11b}$. If an optical pulse is initially distributed among other higher-order modes (for example, LP_{02}, LP_{03}), a soliton including the first 3 modes only will separate temporally from the other modes, while the higher-order modes will compose a nonsoliton, dispersive residual pulse.

From the above considerations, large differences are found between MM solitons and their single-mode counterpart. The former exhibits a fixed pulsewidth at a given wavelength, and possesses an optimal long-range energy; the latter may assume any possible pulsewidth, depending on the input energy. MM solitons do not maintain the initial modal distribution, and transfer all of the energy to the fundamental mode at large propagation distances.

Finally, from Eq. (1.41) we find that a multimode soliton, including nondegenerate modes, cannot exist with pulsewidths T_s larger than a few hundreds of femtoseconds. For picosecond pulses, which are typical of telecom applications, the condition of Eq. (1.40) cannot hold; the N composing modes separate temporally without forming a MM soliton. If a proper energy, given by Eq. (1.33), is provided to the individual N-modes with effective waist $w_e^{(n)}$, it is still possible to observe the formation of N independent single-mode solitons [52].

1.5 CONCLUSIONS

In conclusion, in Sec. 1.2, we discussed the basic properties of guided modes in optical fibers, by comparing two relevant examples: the GIF and the SIF. In order to inspect their mode properties, we calculated their eigenmodes and eigenvalues, based on their different refractive index distribution. By comparing the properties of these fibers, we highlighted the excellent properties of GIFs, such as: smaller effective mode area leading to higher nonlinearity; smaller effective mode area for lower-order modes, favoring self-cleaning of the beam; small group velocity difference between modes, thus favoring the formation of MM solitons; equally-spaced mode phase differences, leading to the self-imaging effect and parametric sideband generation. Finally, we introduced the model of the generalized multimode nonlinear Schrödinger equations, that can effectively describe the evolution of ultrashort pulses in fibers.

In Sec. 1.3, we have revisited the formation of spatio-temporal solitons (STS), also known as light bullets, in a MMF with a parabolic refractive index profile. By using a variational approach, and considering an STS ansatz [see Eq. 1.19], it was possible to derive a set of Euler-Lagrange equations for describing the evolution of the ansatz parameters along the bullet propagation. The fixed points of these equations lead to shape-preserving STSs. These fixed points, their bifurcation diagrams and stability, have been studied in two different regimes. First, we focused on the anti-guiding, self-focusing configuration with anomalous GVD. Here two branches of STS solution exist as a function of the soliton energy E, one unstable and another one neutrally stable, which are connected via a SN bifurcation [see Fig. 1.4]. This point limits the region of existence of the STSs. In a guiding, self-defocusing configuration with normal GVD, only one single STS branch exists, corresponding to a center equilibrium of the reduced dynamical system [see Fig. 1.5]. This STS is neutrally stable, and small perturbations around it lead to a spatio-temporal breather.

Finally, in Sec. 1.4 we theoretically discussed the soliton solutions to the generalized nonlinear Schrödinger equations, for both single-mode and multimode fibers. Soliton formation was described by numerical solutions of the equations and by comparing theory with experimental results. Multimode solitons form whenever the characteristic lengths of chromatic dispersion, modal dispersion, and Kerr nonlinearity are equal to each-other. As a result, an optical pulse propagates with $sech$ temporal shape, where the temporal broadening induced by chromatic dispersion, and delay between modes caused by modal dispersion, are both balanced by Kerr nonlinearity.

The transverse profile of the beam is initially composed by the superposition of different modes, and eventually it undergoes periodic oscillations of the beam waist. After a fiber distance corresponding to hundreds of nonlinear lengths, the modal coupling due to IM-FWM and IM-SRS causes an irreversible transfer of energy from the higher-order modes into the fundamental one. Hence, the multimode soliton gradually converges to a single-mode, fundamental soliton. The initial pulsewidth of the multimode soliton shows invariant properties with respect to the input conditions, and only depends on the input wavelength; its initial pulsewidth is of the order of hundreds of femtoseconds. Hence, we may conclude that the process of multimode soliton formation is always unavoidably affected by both Raman and Kerr nonlinearities.

ACKNOWLEDGEMENT

This work was supported by European Research Council (740355), Marie Sklodowska-Curie Actions (101064614, 101023717), European Research Council 2022-POC2 (101081871), Ministero dell'Istruzione, dell'Universita e della Ricerca (R18SPB8227), Sapienza University of Rome (AR22117A7B01A2EB, AR22117A8AFEF609, RG12117A84DA7437)

BIBLIOGRAPHY

[1] Malitson IH. Interspecimen Comparison of the Refractive Index of Fused Silica. JOSA, Vol 55, Issue 10, pp 1205-1209. 1965 oct;55(10):1205-9.

[2] Fallahkhair AB, Li KS, Murphy TE. Vector Finite Difference Modesolver for Anisotropic Dielectric Waveguides. Journal of Lightwave Technology, Vol 26, Issue 11, pp 1423-1431. 2008 jun;26(11):1423-31.

[3] Krupa K, Tonello A, Shalaby BM, Fabert M, Barthélémy A, Millot G, et al. Spatial beam self-cleaning in multimode fibres. Nature Photonics. 2017 4;11:237-41.

[4] Mangini F, Ferraro M, Zitelli M, Niang A, Mansuryan T, Tonello A, et al. Helical plasma filaments from the self-channeling of intense femtosecond laser pulses in optical fibers. Optics Letters. 2022 1;47:1-4.

[5] Mangini F, Gervaziev M, Ferraro M, Kharenko DS, Zitelli M, Sun Y, et al. Statistical mechanics of beam self-cleaning in GRIN multimode optical fibers. Optics Express. 2022 3;30:10850.

[6] Zitelli M, Ferraro M, Mangini F, Wabnitz S. Single-mode spatiotemporal soliton attractor in multimode GRIN fibers. Photonics Research. 2021;9:741.

[7] Zitelli M, Mangini F, Ferraro M, Sidelnikov O, Wabnitz S. Conditions for walk-off soliton generation in a multimode fiber. Communications Physics. 2021;4:1-6.

[8] Sun Y, Zitelli M, Ferraro M, Mangini F, Parra-Rivas P, Wabnitz S. Multimode soliton collisions in graded-index optical fibers. Opt Express. 2022 Jun;30(12):21710-24.

[9] Hansson T, Tonello A, Mansuryan T, Mangini F, Zitelli M, Ferraro M, et al. Nonlinear beam self-imaging and self-focusing dynamics in a GRIN multimode optical fiber: theory and experiments. Optics Express, Vol 28, Issue 16, pp 24005-24021. 2020 aug;28(16):24005-21.

[10] Ferraro M, Mangini F, Zitelli M, Tonello A, De Luca A, Couderc V, et al. Femtosecond nonlinear losses in multimode optical fibers. Photonics Research. 2021;9(12):2443-53.

[11] Ferraro M, Mangini F, Sun Y, Zitelli M, Niang A, Crocco MC, et al. Multiphoton ionization of standard optical fibers. Photonics Research. 2022;10(6):1394-400.

[12] Wright LG, Wabnitz S, Christodoulides DN, Wise FW. Ultrabroadband Dispersive Radiation by Spatiotemporal Oscillation of Multimode Waves. Physical Review Letters. 2015 11;115:1-5.

[13] Krupa K, Tonello A, Barthélémy A, Couderc V, Shalaby BM, Bendahmane A, et al. Observation of Geometric Parametric Instability Induced by the Periodic Spatial Self-Imaging of Multimode Waves. Physical Review Letters. 2016;116:1-5.

[14] Horak P, Poletti F. Multimode Nonlinear Fibre Optics: Theory and Applications. Recent Progress in Optical Fiber Research. 2012;3(May):3-25.

[15] Wright LG, Ziegler ZM, Lushnikov PM, Zhu Z, Eftekhar MA, Christodoulides DN, et al. Multimode nonlinear fiber optics: Massively parallel numerical solver, tutorial, and outlook. IEEE Journal of Selected Topics in Quantum Electronics. 2018;24(3):1-16.

[16] Stolen RH, Tomlinson WJ, Haus HA, Gordon JP. Raman response function of silica-core fibers. Journal of the Optical Society of America B. 1989;6(6):1159.

[17] Agrawal GP. Nonlinear fiber optics. Fifth edit ed. Academic press; 2013.

[18] Zitelli M, Mangini F, Ferraro M, Niang A, Kharenko D, Wabnitz S. High-energy soliton fission dynamics in multimode GRIN fiber. Optics Express. 2020;28(14):20473-88.

[19] Kivshar YS, Agrawal GP, Kivshar YS. Optical Solitons: From Fibers to Photonic Crystals. Amsterdam ; Boston: Academic press; 2003.

[20] Silberberg Y. Collapse of optical pulses. Optics Letters. 1990 Nov;15(22):1282-4. Publisher: Optica Publishing Group.

[21] Carretero-González R, Frantzeskakis DJ, Kevrekidis PG. Nonlinear waves in Bose–Einstein condensates: physical relevance and mathematical techniques. Nonlinearity. 2008

Jul;21(7):R139-202.
[22] Malomed BA. Variational methods in nonlinear fiber optics and related fields. In: Progress in Optics. vol. 43. Elsevier; 2002. p. 71-193.
[23] Pérez-García VM, Michinel H, Cirac JI, Lewenstein M, Zoller P. Dynamics of Bose-Einstein condensates: Variational solutions of the Gross-Pitaevskii equations. Physical Review A. 1997 Aug;56(2):1424-32.
[24] Raghavan S, Agrawal GP. Spatiotemporal solitons in inhomogeneous nonlinear media. Optics Communications. 2000 Jun;180(4):377-82.
[25] Doedel EJ, Keller HB, Kernevez JP. Numeri- cal analysis and control of bifurcation problems (i): bi- furcation in finite dimensions. Int Journal Bifurcation Chaos Appl Sci Eng. 1991;01(03):493-520.
[26] Doedel EJ, Oldeman BE, Champneys AR, Dercole F, Fairgrieve T, Kuznetsov YA, et al. AUTO-07p: Software for continuation and bifurcation problems in ordinary differential equations. Department of Computer Science, Concordia University, Montreal. 2007.
[27] Yu SS, Chien CH, Lai Y, Wang J. Spatio-temporal solitary pulses in graded-index materials with Kerr nonlinearity. Optics Communications. 1995 Aug;119(1):167-70.
[28] Wiggins S. Introduction to Applied Nonlinear Dynamical Systems and Chaos. 2nd ed. Springer, New York; 2003.
[29] Agrawal GP. In: Fiber-Optic Communication Systems. New York: Wiley; 2010. p. Ch. 2.
[30] Zakharov VE, Shabat AB. Exact theory of two-dimensional self-focusing and one-dimensional self-phase modulation of waves in nonlinear media. Sov Phys JEPT. 1972;34.
[31] Wabnitz S. In: Chesnoy J, editor. Undersea Fiber Communication Systems. Academic Press; 2015. .
[32] Hasegawa A, Matsumoto M. In: Optical Solitons in Fibers. Berlin, Heidelberg: Springer Berlin Heidelberg; 2003. p. 41-59.
[33] Zakharov VE, Wabnitz S. In: Optical Solitons: Theoretical Challenges and Industrial Perspectives. Berlin, Heidelberg: Springer Berlin Heidelberg; 1999. .
[34] Hasegawa A, Kodama Y. Guiding-center soliton. Physical Review Letters. 1991;66(2):161-4.
[35] Raghavan S, Agrawal GP. Spatiotemporal solitons in inhomogeneous nonlinear media. Optics Communications. 2000;180(4):377-82.
[36] Renninger WH, Wise FW. Optical solitons in graded-index multimode fibres. Nature Communications. 2013;4.
[37] Manassah JT, Baldeck PL, Alfano RR. Self-focusing and self-phase modulation in a parabolic graded-index optical fiber. Optics Letters. 1988;13(7):589-91.
[38] Karlsson M, Anderson D, Desaix M. Dynamics of self-focusing and self-phase modulation in a parabolic index optical fiber. Optics Letters. 1992;17(1):22-4.
[39] Ahsan AS, Agrawal GP. Graded-index solitons in multimode fibers. Optics Letters. 2018;43(14):3345-8.
[40] Mafi A. Pulse Propagation in a Short Nonlinear Graded-Index Multimode Optical Fiber. Journal of Lightwave Technology. 2012;30(17):2803-11.
[41] Mitschke FM, Mollenauer LF. Discovery of the soliton self-frequency shift. Optics Letters. 1986;11(10):659-61.
[42] Gordon JP. Theory of the soliton self-frequency shift. Optics Letters. 1986;11(10):662-4.
[43] Grudinin AB, Dianov EM, Korbkin DV, Prokhorov AMD, Khaidarov V. Nonlinear mode coupling in multimode optical fibers; excitation of femtosecond-range stimulated-Raman-scattering solitons. JEPT Lett. 1988;47(6):356-9.
[44] Ho K, Kahn JM. Linear propagation effects in mode-division multiplexing systems. Journal of Lightwave Technology. 2014;32(4):614-28.

[45] Mumtaz S, Essiambre R, Agrawal GP. Nonlinear propagation in multimode and multi-core fibers: Generalization of the Manakov equations. Journal of Lightwave Technology. 2013;31(3):398-406.

[46] Xiao Y, Essiambre R, Desgroseilliers M, Tulino AM, Ryf R, Mumtaz S, et al. Theory of intermodal four-wave mixing with random linear mode coupling in few-mode fibers. Optics Express. 2014;22(26):32039-59.

[47] Mecozzi A, Antonelli C, Shtaif M. Coupled Manakov equations in multimode fibers with strongly coupled groups of modes. Optics Express. 2012;20(21):23436-41.

[48] Hasegawa A. Self-confinement of multimode optical pulse in a glass fiber. Optics Letters. 1980;5(10):416-7.

[49] Crosignani B, Di Porto P. Soliton propagation in multimode optical fibers. Optics Letters. 1981;6(7):329-30.

[50] Zitelli M, Ferraro M, Mangini F, Wabnitz S. Characterization of Multimode Soliton Self-Frequency Shift. Journal of Lightwave Technology. 2022:1-8.

[51] Zitelli M, Sun Y, Ferraro M, Mangini F, Sidelnikov O, Couderc V, et al. Multimode solitons in step-index fibers. Optics Express. 2022;30(4):6300-10.

[52] Zitelli M, Ferraro M, Mangini F, Wabnitz S. Mode-scrambling security using short pulses in multimode graded-index fiber. In: 2021 AEIT International Annual Conference (AEIT). IEEE; 2021. p. 1-4.